



Cite this: *Nanoscale*, 2018, **10**, 13140

Highly durable and cycle-stable lithium storage based on MnO nanoparticle-decorated 3D interconnected CNT/graphene architecture†

Junyong Wang,^a Cong Wu,^a Qinglin Deng,^a Kai Jiang,^a Liyan Shang,^a Zhigao Hu ^{*a,b} and Junhao Chu^a

To accommodate huge volume change and boost the inferior electrochemical reaction kinetics of manganese oxide anodes for lithium-ion batteries, a unique 3D porous CNT/graphene–MnO architecture has been synthesized, with MnO nanoparticles homogeneously decorated on 3D interconnected CNT/graphene (3DCG) conductive networks. This porous 3DCG matrix with its abundant open pores and large surface area can provide efficient channels for fast charge transport and allow full contact between the electrode and electrolyte, leading to improved electrochemical activity. The robust 3D architecture offers abundant stress buffer space to tolerate volume expansion and ensures robust structural stability during the electrochemical processes. The synergistic effect between components endows the 3DCG/MnO electrodes with excellent electrochemical performance, retaining a high specific capacity of 526.7 mA h g⁻¹ at 2.0 A g⁻¹ with 98% capacity retention over 1400 cycles. This work provides a promising route for the practical application of fast and durable lithium-ion batteries and suggests insights for rational structural designs with other transition metal oxides.

Received 4th March 2018,
Accepted 14th June 2018

DOI: 10.1039/c8nr01835a

rsc.li/nanoscale

1 Introduction

Nowadays, the prosperous development of rapidly improving portable electronic devices, newly emerging electric vehicles, and smart electrical grid storage has motivated an ever-growing demand for efficient energy storage. Lithium-ion batteries (LIBs), merited by their high energy density, low self-discharge, and lack of memory effect, dominate the market for consumer electronic devices.^{1,2} However, the current mainstream LIBs are mainly based on graphite anode materials with low theoretical capacity (372 mA h g⁻¹), which largely limits their large-scale application in burgeoning electronics. Hence, it is imperative to advance new anode materials such as Si,³ Sn,⁴ and transition metal oxides (TMOs) with high capacities and stable cycle performances to obtain better LIBs.⁵ As a subclass of TMO, manganese oxides, particularly MnO, merited by their high theoretical specific capacities,

high theoretical energy densities, low electrochemical motivation force, natural abundance and their environmentally friendly attributes, have attracted extensive attention and are considered to be promising anode materials.^{6–8} Unfortunately, the practical application of manganese oxide is still obstructed by several general problems that must be addressed. For instance, MnO has the high theoretical capacity of 756 mA h g⁻¹, yet suffers from severe capacity degradation driven by large volume expansion and low intrinsic electric conductivity during the electrochemical reaction.⁹ What is more, the utilization of active metal oxides is low on account of the lack of a continuous conductive network and interpenetrated ion transport pathways throughout the whole electrode and these need to be adjusted in order to obtain excellent electrochemical performance for LIB anodes.¹⁰

To date, considerable efforts have been made to solve the above-mentioned obstacles by engineering suitable architectures. One effective strategy is to combine carbonaceous support materials with metal oxides to rationally fabricate various nanostructures, which would take advantage of the high electrical conductivity and flexible characteristics of carbon materials, as well as the high specific capacities of metal oxides. For example, several kinds of dual-carbon decorated nanosized MnO particle have been reported by Mu's group.^{11,12} Li's group synthesized a peapod-like MnO/C heterostructure with decent electrochemical performance.¹³ Yu *et al.*

^aKey Laboratory of Polar Materials and Devices (MOE) and Technical Center for Multifunctional Magneto-Optical Spectroscopy (Shanghai), Department of Electronic Engineering, East China Normal University, Shanghai 200241, China.

E-mail: zghu@ee.ecnu.edu.cn; Fax: +86-21-54345119; Tel: +86-21-54345150

^bCollaborative Innovation Center of Extreme Optics, Shanxi University, Taiyuan, Shanxi 030006, China

†Electronic supplementary information (ESI) available. See DOI: 10.1039/C8NR01835A

also developed a biotemplated route for designing 3D porous architecture for an advanced MnO-based anode.¹⁴ Among various carbon-based materials, 3D structures with excellent flexibility and good structural stability are favorable for alleviating volume expansion and structural damage.^{15,16} An interconnected network with a large surface area and abundant mass-transportation channels inevitably improves the kinetics of electron and ion transfer and the electrochemical activity of metal oxides, since the active materials can make full contact with and store sufficient electrolyte and the electrons can easily be transferred into the continuous pathways.¹⁷ Moreover, the lithium storage behavior of metal oxides can be adjusted to exhibit surface-controlled kinetics in rationally designed carbon-based 3D architectures, leading to unusual rate capability and cycling stability. The above virtues make them good auxiliaries for application in the electrode materials of LIBs. For example, Dou and co-workers fabricated a 3D porous MnO@N-GSC/GR configuration with 1D MnO nanowires sheathed in 2D N-doped graphene ribbons along with N-doped GSCs, and a novel hybrid RGO–MnO–RGO with a sandwich nanostructure, delivering greatly enhanced electrochemical performance.^{18,19}

From the above, to achieve eminent cycle stability and rate capability simultaneously, a highly efficient 3D interconnected architecture with a large surface area and high porosity remains an anode material engineering target. Herein, we demonstrate a highly durable and cycle-stable 3D electrode architecture using graphene and carbon nanotubes (CNTs) as the conductive scaffold, which themselves are synchronously decorated with ultrafine manganous oxide (MnO) nanoparticles, namely, 3DCG/MnO (as shown in Scheme 1). In the resulting 3DCG/MnO architecture, the highly interconnected conductive matrix in the 3DCG provides excellent electron transport properties, and its porous structure facilitates rapid ion transport and mitigates diffusion limitations throughout the entire electrode architecture. At the same time, the purposely generated manganous oxide nanoparticles to ensure the stable formation of a solid electrolyte interface, which avoids atom migration and enhances the structural integrity during cycling, leading to spatially confined electrochemical reac-

tions. This 3D porous MnO-based material with its novel structure exhibits a reversible capacity of 526.7 mA h g⁻¹ over 1400 cycles under a high current density of 2.0 A g⁻¹ (corresponding to a capacity retention of 98%), along with superior rate capability, and displays strong potential as an advanced anode for the practical application of LIBs.

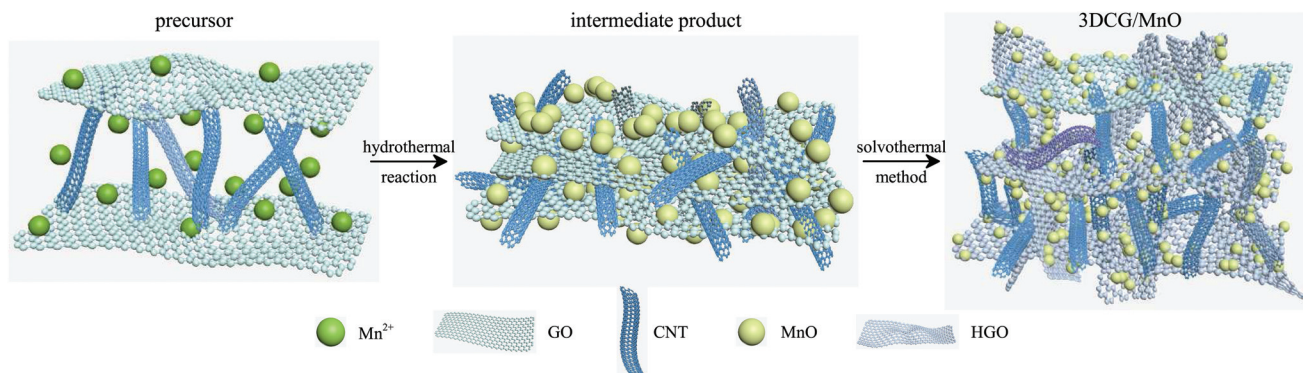
2 Experimental

2.1 Material preparation

Graphene oxide (GO) was prepared from natural graphite powder using the Hummer's approach. CNTs were obtained from XFNANO Materials Tech Co., Ltd (Nanjing, China). The 3DCG/MnO architecture was prepared using a hydrothermal method and a subsequent solvothermal process, as shown in Scheme 1. In the first synthesis step, 1 mmol of Mn(Ac)₂·4H₂O and 4 g of NaOH were dissolved in a solution of 60 mL of de-ionized water, 20 mg of CNTs, and 60 mg of GO, which was then transferred to a 100 mL Teflon-lined autoclave. After heating at 180 °C for 12 h, the reactants were centrifuged and washed with deionized water and absolute alcohol. The intermediate product was obtained by vacuum drying at 60 °C for 12 h and post-annealing at 600 °C for 2 h in an Ar atmosphere. To obtain the highly porous 3DCG/MnO composite, 10 mg of graphene oxide was dissolved in a solution of 30 mL of de-ionized water and 1 mL of H₂O₂ at 95 °C for 2 h to obtain a HGO aqueous dispersion. In the second synthesis step, 48 mg of the intermediate product was added to the HGO solution, which was followed by a reduction process at 100 °C with constant stirring and post-annealing at 600 °C for 2 h in an Ar atmosphere to produce the final product with 3DCG/MnO architecture. For comparison, bare MnO was synthesized using a one-step hydrothermal method without the conductive material additive.

2.2 Materials characterization

X-ray diffraction (XRD) analysis was carried out on a Bruker D8 diffractometer equipped with Cu-K α radiation ($\lambda = 0.154$ nm) at a generator voltage of 40 kV and a generator current of



Scheme 1 Schematic illustration of the formation of the 3DCG/MnO architecture.

20 mA. Raman scattering measurement was carried out using a micro-Raman spectrometer (Jobin-Yvon LabRAM HR 800UV) with an excitation laser beam wavelength of 632.8 nm. X-ray photoelectron spectroscopy (XPS) was conducted on a RBD upgraded PHI-5000C ESCA system (PerkinElmer) with Mg-K α radiation ($h\nu = 1253.6$ eV). Scanning electron microscopy (SEM) images were obtained using PHILIPS XL30TMP. Transmission electron microscopy (TEM) and high-resolution TEM (HRTEM) were performed on an FEI Tecnai G20 TEM, operated at 200 kV. Nitrogen adsorption/desorption isotherms, Brunauer-Emmett-Teller (BET) surface areas and DFT pore size distributions were measured using a TriStar II 3020 instrument. Thermogravimetric analysis (TGA) was carried out using TA instruments with a ramp rate of 10 °C min⁻¹ under 50 mL min⁻¹ of flowing air.

2.3 Electrochemical measurements

Electrochemical characterization was conducted using 2025-type coin cells. All cell assemblies were carried out in an Argon-filled glovebox with the concentrations of moisture and oxygen below 1 ppm. To prepare the working electrodes, a slurry of the active materials (3DCG/MnO), carbon black, and polyvinylidene fluoride with a mass ratio of 80 : 10 : 10 in *N*-methyl-2-pyrrolidone was uniformly coated on a copper foil and then dried in a vacuum oven at 100 °C for 12 h. Lithium metal was used as the counter electrode and the separator was a Cellgard 2400 polypropylene membrane. The electrolyte was 1 M LiPF₆ dissolved in ethylene carbonate, dimethyl carbonate, and ethyl methyl carbonate (1 : 1 : 1, in vol.). Galvanostatic

charge-discharge tests were conducted on a Land CT 2001A battery testing system in the potential window between 0.02 and 3.0 V (vs. Li/Li⁺). Cyclic voltammetry (CV) and electrochemical impedance spectroscopy (EIS) tests were recorded on a CHI660D electrochemical workstation. CV experiments were carried out between 0.02 and 3.0 V and EIS measurements were carried out in the frequency range between 0.01 Hz and 100 kHz with an amplitude of 5 mV. For comparison, bare MnO was tested as an electrode by the same process.

3 Results and discussion

The 3DCG/MnO composite was successfully fabricated through a two-step process, in which MnO nanoparticles were incorporated into a 3D architecture consisting of graphene oxide (GO) and carbon nanotubes (CNTs). The X-ray diffraction (XRD) pattern of 3DCG/MnO is displayed in Fig. 1a. The diffraction peaks reveal that the dominant phase of the sample is face-centered cubic (fcc) MnO with the *Fmm* space group (JCPDS no. 07-0230). Additionally, the broad diffraction peak centered around 25° corresponds to the (002) plane of graphitic carbon, and is a characteristic peak of hexagonal graphite (JCPDS no. 41-1487).¹⁹ This result indicates that most of the GO had been reduced to graphene after the preparation process, as also proven by X-ray photoelectron spectroscopy (XPS) at the C 1s region (Fig. 1b). Clearly, the peak related to the oxidized carbon species (C–O, 286.7 eV) is negligible compared to the dominant peak for C–C (284.5 eV) in the high-

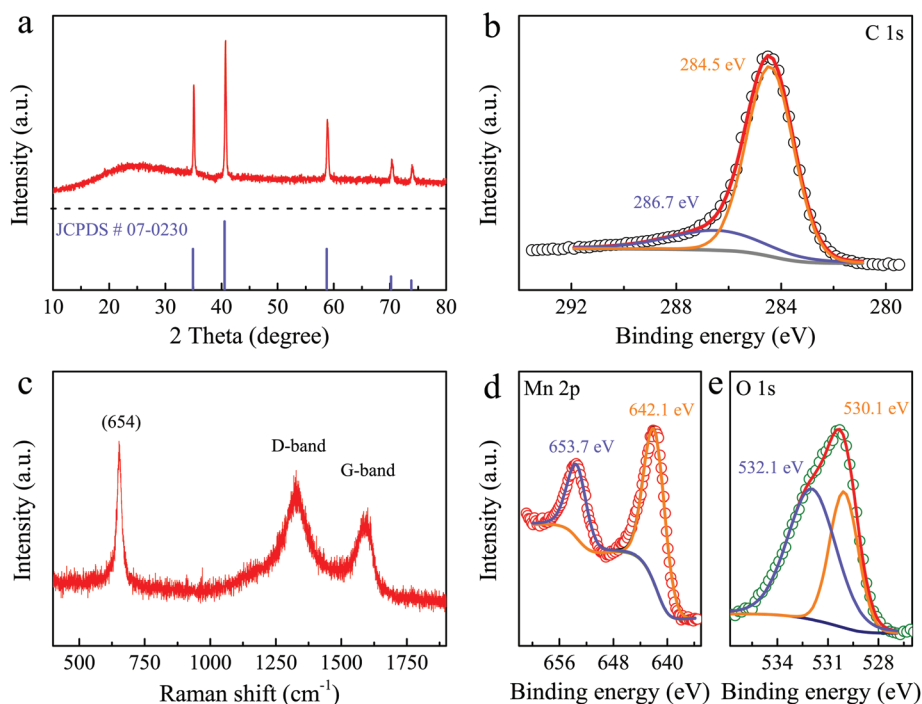


Fig. 1 (a) XRD patterns; (b) high-resolution XPS spectra of C 1s; (c) Raman spectra; (d) high-resolution XPS spectra of Mn 2p and (e) high-resolution XPS spectra of O 1s for the 3DCG/MnO composite.

resolution C 1s XPS spectrum of 3DCG/MnO. Raman spectroscopy was further employed to investigate the graphitization degree of the composite, as shown in Fig. 1c. The Raman spectrum contains a D band at 1328 cm^{-1} (the defect-induced mode from disordered carbon) and a G band at 1592 cm^{-1} (the sp^2 -hybridized graphitic mode).²⁰ The intensity ratio of the D versus the G band (I_D/I_G) is demonstrative of the degree of graphitic disorder. The I_D/I_G value, which represents the structural imperfection of sp^3 -type disordered carbon materials with numerous defects,¹² is large for 3DCG/MnO (1.24), which is consistent with the XRD and XPS results. Meanwhile, the Raman peak at 654 cm^{-1} corresponds to the vibration of the Mn–O bonds.²¹ The formation of the MnO phase was also confirmed by the high-resolution Mn 2p XPS spectrum (Fig. 1d); the spin-energy separation of 11.6 eV for the Mn 2p doublet indicates an oxidation state of Mn^{2+} . Furthermore, the two prominent peaks with binding energies 642.1 and 653.7 eV, which were best fitted using the Gaussian fitting method, correspond to the typical Mn $2\text{p}^{3/2}$ and $2\text{p}^{1/2}$ spin orbits and are in good agreement with those reported for

MnO .^{22,23} The high-resolution XPS spectrum of O 1s in Fig. 1e is deconvoluted into two peaks. Typically, a peak at 530.1 eV corresponds to Mn–O bonds and the peak at 532.1 eV can be assigned to C–O, indicating the existence of defects, contaminants, and chemisorbed oxygen surface species.¹¹

The morphology and structure of the 3DCG/MnO composite were investigated using scanning electron microscopy (SEM). Obviously, the as-prepared composite possesses an interconnected 3D porous architecture, as shown in Fig. 2a and Fig. S1.† The pore size ranges from a few hundred nanometers to several micrometers. The magnified SEM images (Fig. 2b and Fig. S2†) reveal that MnO nanoparticles with a uniform size are homogeneously embedded in the 3D cross-linked CNT/graphene nanoframework. Nitrogen adsorption–desorption analysis confirms the high Brunauer–Emmett–Teller (BET) specific surface area ($128\text{ m}^2\text{ g}^{-1}$) of 3DCG/MnO and the existence of a mass of meso- and macropores (Fig. 2c), matching well with observations from the SEM images. A characteristic structure such as this with a high specific surface area and abundant pores is beneficial for the permeation and transpor-

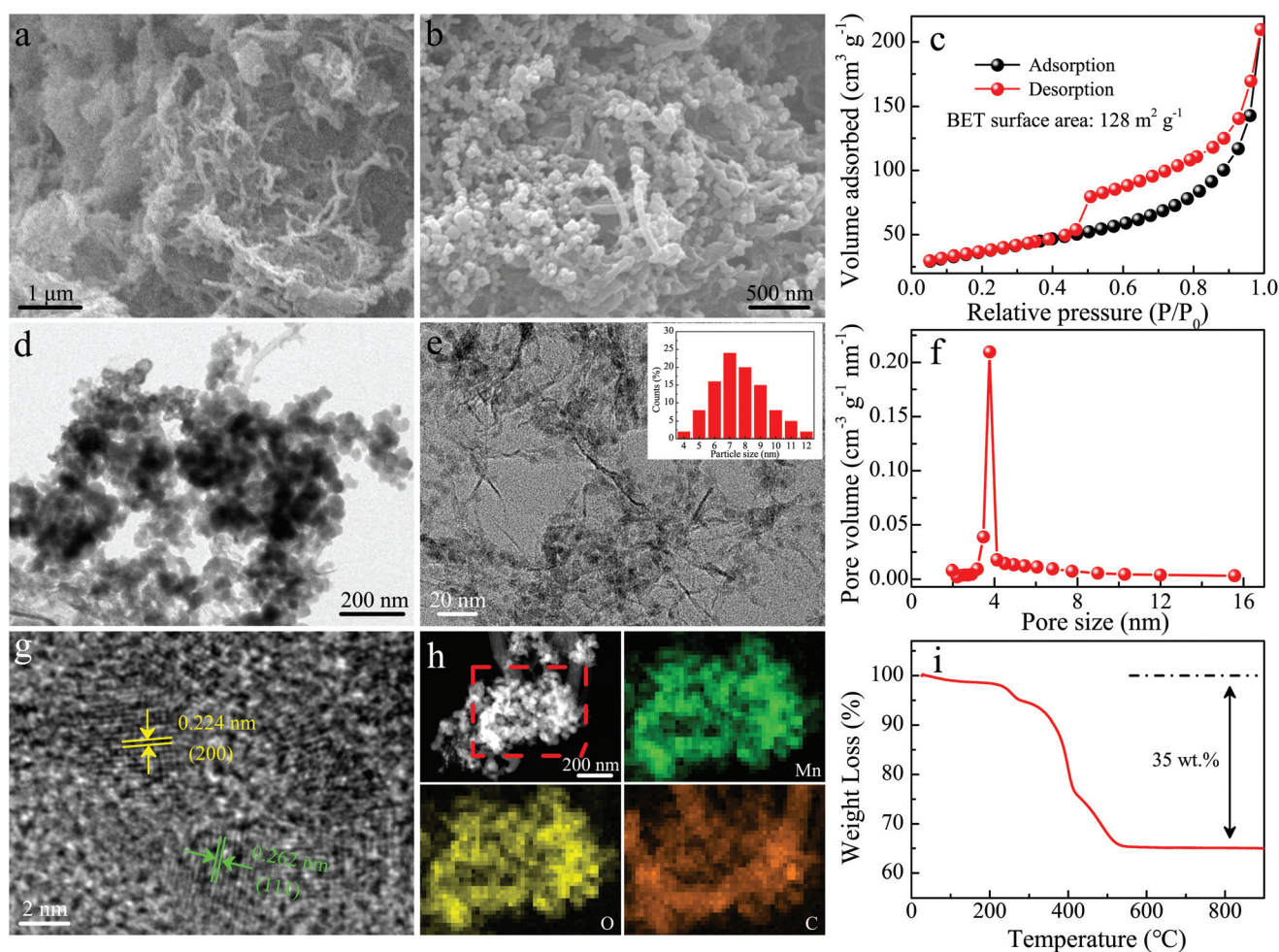


Fig. 2 Morphological and structural characterizations of the 3DCG/MnO composite: (a and b) SEM images; (c) N_2 adsorption–desorption isotherms; (d) low magnification TEM image; (e) high magnification TEM image, the inset shows the particle distribution; (f) pore size distribution curve; (g) HRTEM image; (h) TEM image and corresponding EDS mapping; (i) TGA curve.

tation of lithium ions as well as the accommodation of the volumetric change in the MnO nanoparticles during cycling. The interconnected structure of the 3DCG/MnO composite was further confirmed using transmission electron microscopy (TEM), as shown in Fig. 2d and Fig. S3.† It can be seen that MnO consists of small sized particles. A histogram of the particle size was obtained from random regions of a high magnitude TEM image (Fig. 3e). It shows a small average particle size with a relatively narrow size distribution, which may be attributed to the presence of graphene and carbon nanotubes. The pore size distribution curve in Fig. 2f suggests that the micropores are distributed around 4 nm in 3DCG/MnO, in good agreement with observations from the SEM and TEM images. The high-resolution TEM (HRTEM) image in Fig. 2g reveals that each MnO nanoparticle exhibits single crystalline features with lattice fringes of $d = 0.224$ and 0.262 nm, corresponding to the (200) and (111) facets of cubic-phase MnO, respectively. Specifically, the TEM image with the corresponding energy dispersive spectrometry (EDS) elemental

mapping (Fig. 2h) further verify the homogeneous distribution of Mn, O, and C elements in the 3DCG/MnO composite. To determine the content of manganous oxide, thermogravimetric analysis (TGA) was performed in air, as shown in Fig. 2i. From a 7.5 wt% increase in weight when MnO was oxidised to Mn_3O_4 ,¹⁹ manganous oxide was determined to be about 60.5 wt% in the 3DCG/MnO composite.

The electrochemical behavior of 3DCG/MnO as an anode material has been investigated in half-cell LIBs. All of the electrochemical measurements were tested in the potential range 0.02–3.0 V *versus* Li/Li⁺. Fig. 3a shows the cyclic voltammogram (CV) curves for the first five consecutive cycles for the 3DCG/MnO electrode at a scan rate of 0.5 mV s^{-1} . In the first cathodic scan, the sharp peak at 0.07 V corresponds to the initial reduction of MnO ($\text{MnO} + 2\text{Li}^+ + 2\text{e}^- \rightarrow \text{Mn} + \text{Li}_2\text{O}$), and the broad peak located at 0.56 V disappearing after subsequent cycles indicates the formation of a solid electrolyte interface (SEI) film with the irreversible reduction of the electrolyte.^{13,22} In the first anodic scan, one peak at 1.27 V can be observed,

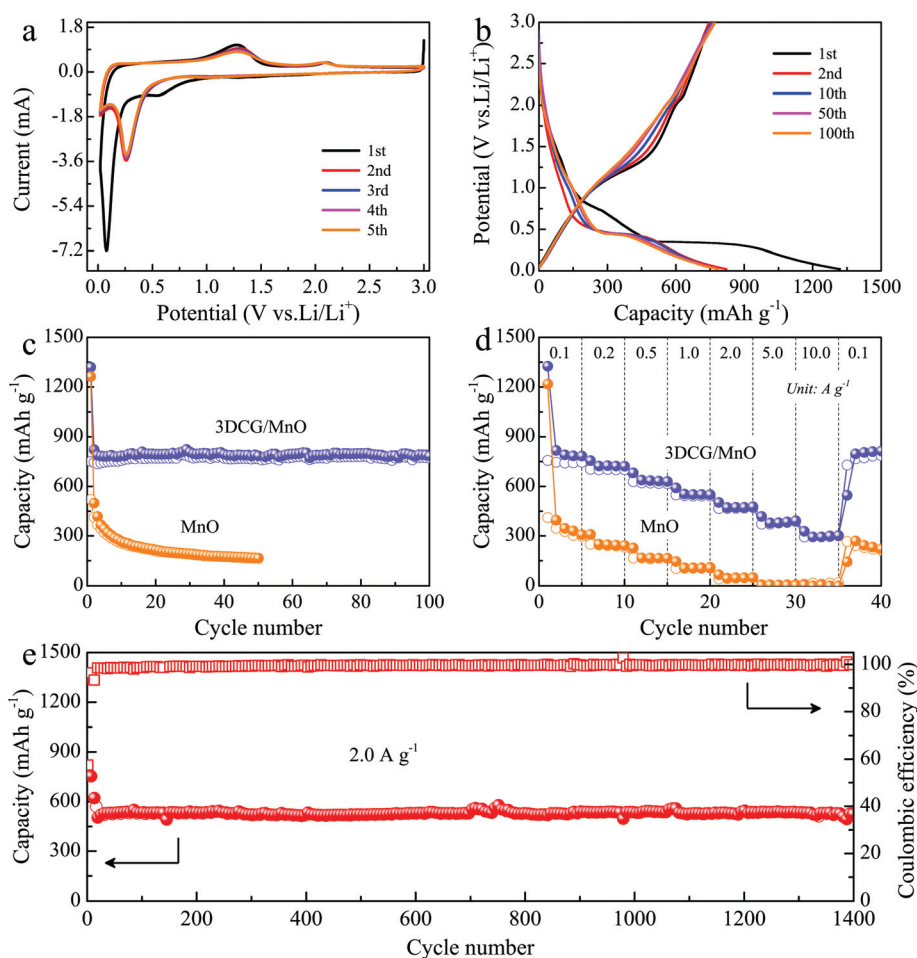


Fig. 3 Electrochemical properties of the 3DCG/MnO composite: (a) CV curves of the 3DCG/MnO electrode at a scan rate of 0.5 mV s^{-1} ; (b) galvanostatic charge–discharge profiles of the 3DCG/MnO electrode at 0.1 A g^{-1} ; (c) cycling stability of the 3DCG/MnO and MnO electrodes at 0.1 A g^{-1} ; (d) rate capability of the 3DCG/MnO and MnO electrodes at various current densities of 0.1 – 10 A g^{-1} ; (e) long-term cycling stability and coulombic efficiency of 3DCG/MnO at the high current density of 2.0 A g^{-1} .

corresponding to the reversible oxidation of metallic Mn to Mn^{2+} ($\text{Mn} + \text{Li}_2\text{O} \rightarrow \text{MnO} + 2\text{Li}^+ + 2\text{e}^-$).⁶ Another weak oxidation peak appears at 2.07 V, which corresponds to the further oxidation of Mn^{2+} to a higher oxidation state. This may boost the charge transfer kinetics and the electrochemical activity derived from the structure evolution of the 3DCG/MnO electrode.^{18,24,25} Notably, the aforementioned peaks at 0.07 and 1.27 V shift to 0.25 and 1.31 V in the subsequent sweeps, respectively. This shift in peak position to a higher potential demonstrates the enhanced kinetics and the irreversible structure reconstruction stimulated by the formation of Li_2O and metallic manganese after the initial discharge-charge processes.^{11,26,27} The subsequent CV curves overlap well with each other for 2–5 cycles, suggesting a relatively stable cycling process with good reversibility and capacity retention for the 3DCG/MnO electrode. For comparison, the initial five CV curves of the MnO electrode are displayed in Fig. S4,† which exhibits similar electrochemical characteristics to 3DCG/MnO. However, there being only the peak at 1.28 V in the anodic scan without further oxidation of Mn^{2+} indicates the sluggish reaction kinetics of bare MnO.

Fig. 3b presents the galvanostatic charge-discharge profiles of the 3DCG/MnO electrode for the 1st, 2nd, 10th, 50th, and 100th cycles at a current density of 0.1 A g^{-1} . In accordance with the CV curves, distinct plateaus at around 0.5 V and 1.2 V in the discharge and charge profiles can be observed, corresponding to the reduction and oxidation of Mn^{2+} and Mn, respectively. The first discharge and charge capacities of the 3DCG/MnO electrode are 1319.9 and $751.1 \text{ mA h g}^{-1}$, respectively, acquiring an initial coulombic efficiency of 56.9%, which is much higher than that of bare MnO (41.3%, Fig. 3c). The initial irreversible capacity loss is attributed to the formation of the SEI layer and the decomposition of the electrolyte, as well as the irreversible insertion of lithium ions into the defects on the carbon network.^{6,10,12} Such phenomena are generally observed in conversion electrode materials such as TMOs and transition metal sulfides,^{28–30} and could be solved by prelithiation techniques or the incorporation of sacrificial Li salt additives.^{31,32} However, the coulombic efficiency rapidly increases to about 97% after several cycles, suggesting the rapid stabilization of the SEI film. Moreover, the discharge capacity slightly decreases to $788.7 \text{ mA h g}^{-1}$ after the first two cycles, yet could be maintained for the subsequent 100 cycles ($784.3 \text{ mA h g}^{-1}$ after 100 cycles) (Fig. 3c). In contrast, although MnO delivers a relatively high initial discharge capacity of $1262.2 \text{ mA h g}^{-1}$, its discharge capacity attenuates sharply with only around $166.2 \text{ mA h g}^{-1}$ maintained after 50 cycles (Fig. 3c). Note that the specific capacity of 3DCG/MnO is higher than the theoretical capacity of MnO (756 mA h g^{-1}), which may be attributed to the extra lithium storage due to the further oxidation of Mn^{2+} to a higher oxidation state and/or the formation of a polymeric gel-type layer.^{17,27} The above results fully demonstrate that the integration of MnO nanoparticles into 3DCG with an interconnected porous structure largely improves the electrochemical performance of a MnO-based anode material.

The high rate capability and cycle stability of the 3DCG/MnO electrode were further explored for the potential application of the electrode in next generation LIBs. As shown in Fig. 3d, the reversible capacity fell moderately when increasing the current density from 0.1 to 10.0 A g^{-1} . The 3DCG/MnO electrode could deliver average reversible capacity values of 783.5, 721.8, 630.0, 550.2, and $477.6 \text{ mA h g}^{-1}$ at 0.1, 0.2, 0.5, 1.0, and 2.0 A g^{-1} , respectively, which are superior to those of bare MnO. Even at the high current density values of 5.0 and 10.0 A g^{-1} , the average reversible capacity was still maintained at as high as 393.0 and $302.8 \text{ mA h g}^{-1}$, respectively. Notably, a reversible high capacity of $814.6 \text{ mA h g}^{-1}$ was swiftly restored when the current density was reversed back to 0.1 A g^{-1} after high-rate charging-discharging at 10 A g^{-1} , highlighting the strong tolerance for fast reactions and the good lithium storage reversibility of the 3DCG/MnO electrode. From the charge-discharge profiles (Fig. S5†), it can be seen that the 3DCG/MnO electrode shows much lower polarization than bare MnO, indicating enhanced electrochemical reaction kinetics. In addition to the impressive rate capability, 3DCG/MnO is also endowed with excellent cycling stability. The cycling performance and corresponding coulombic efficiency at a current density of 0.5 A g^{-1} are shown in Fig. S6.† The 3DCG/MnO electrode achieved an initial charge capacity of $766.1 \text{ mA h g}^{-1}$ and had outstanding cycle stability. Impressively, nearly 100% coulombic efficiency throughout the overall cycling range could be stably achieved. Even after 400 cycles, a charge capacity of $773.0 \text{ mA h g}^{-1}$ could be attained, which is still higher than the theoretical capacity of MnO. Furthermore, the 3DCG/MnO electrode exhibited an impressive cycle lifespan at a high current density of 2.0 A g^{-1} (Fig. 3e). After the activation process in the initial 16 cycles, its reversible discharge capacity changed from 535.6 to $526.7 \text{ mA h g}^{-1}$ at 2.0 A g^{-1} for the 17th and 1400th cycles, respectively. The mean capacity loss was only 0.006% per cycle, which is further evidence for its superior cycle stability. Compared to other previously reported TMO/carbon hybrid anode materials, the 3DCG/MnO anode exhibited excellent long-term cycling stability even under fast and deep discharge-charge processes, as summarized in Table S1.† The excellent rate performance and remarkable cycle stability of the 3DCG/MnO electrode can be attributed to the rationally designed hybrid configuration, which may be due to the synergistic effect of the ultrafine MnO nanoparticles and the interconnected conductive nanoframeworks.

The superior electrochemical performance of 3DCG/MnO draws our attention to understanding the origin of the improved electrochemical kinetics. Therefore, CV and electrochemical impedance spectroscopy (EIS) tests were conducted. Fig. 4a displays the CV curves of a fresh 3DCG/MnO electrode at the various scan rates of 0.1, 0.3, 0.5, 0.7, and 1.0 mV s^{-1} . The shape was well preserved when increasing the scan rate from 0.1 to 1.0 mV s^{-1} . Moreover, the peak voltage shift with the scan rate for 3DCG/MnO, which is less than that for bare MnO (Fig. S7†), suggests a smaller degree of polarization and faster reaction kinetics of the 3DCG/MnO electrode. The degree of capacitive effect can be qualitatively analyzed accord-

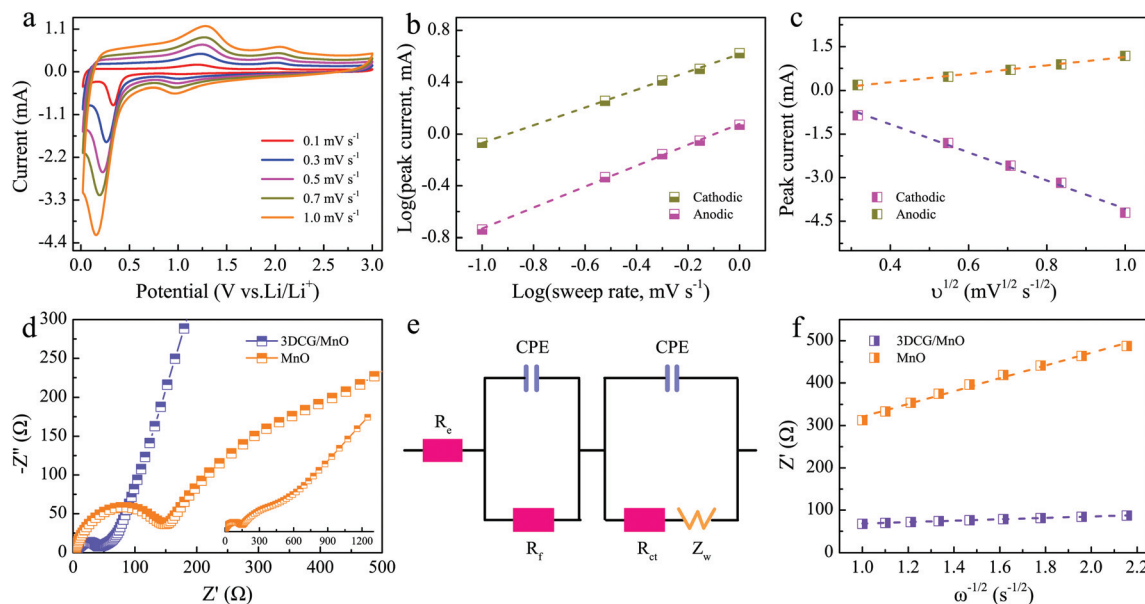


Fig. 4 Kinetic analysis of the electrochemical behavior of the 3DCG/MnO electrode: (a) CV curves of the 3DCG/MnO electrode at various scan rates from 0.1 to 1.0 mV s^{-1} ; (b) determination of the b value using the relationship between the peak current and the scan rate; (c) the linear relationship between the peak current and the square root of the scan rate; (d) EIS curves of the 3DCG/MnO and bare MnO electrodes; (e) the corresponding equivalent circuit; (f) the Warburg impedance of the 3DCG/MnO and MnO electrodes.

ing to the relationship between the measured current (i) and the scan rate (ν) from the CV curves:³³

$$i = a\nu^b \quad (1)$$

where a and b are adjustable values. The b value reflects the control process of the electrochemical behavior, which can be determined from the slopes of the plots of $\log(i)$ versus $\log(\nu)$, as shown in Fig. 4b. Generally, a b value of 0.5 represents an ideal diffusion-controlled process, whereas 1.0 represents an ideal surface-controlled process. Hence, the higher b values of the 3DCG/MnO electrode (0.69 vs. 0.52 for the bare MnO electrode at the cathodic peak and 0.81 vs. 0.5 for the bare MnO electrode at the anodic peak, Fig. S8†), explicitly indicate that the kinetics of the redox reactions between MnO and Mn^{2+} are primarily surface-controlled, giving rise to the correspondingly fast kinetics of capacitive storage. The lithium ion diffusion coefficient of the 3DCG/MnO electrode during the charge–discharge process was further revealed by CV profiles at different sweep rates, as shown in Fig. 4c. The peak current (I_{pc}) of the intensive cathodic/anodic peaks at 0.3/1.25 V is in linear response to the square root of the sweep rate ($\nu^{1/2}$), from which the apparent lithium ion diffusion coefficient can be further estimated according to the Randles–Sevcik equation:^{34,35}

$$I_{\text{pc}} = 2.69 \times 10^5 \times n^{3/2} A D^{1/2} C \nu^{1/2} \quad (2)$$

where I_{pc} is the peak current and ν is the sweep rate. n represents the number of electrons involved in the half-reaction and A is the total surface area of the 3DCG/MnO electrode. C corresponds to the molar concentration of lithium ions in MnO and D is the lithium ion diffusion coefficient in MnO at

298 K. Fig. 4c shows a linear relationship between the peak current (I_{pc}) and the square root of the sweep rate ($\nu^{1/2}$) in the cathodic and anodic processes, in which the slope of the fitted linear dashed line can be used to calculate the D values. According to eqn (1), the lithium ion diffusion coefficients for 3DCG/MnO can be estimated to be 1.39×10^{-12} and $1.25 \times 10^{-13} \text{ cm}^2 \text{ s}^{-1}$ for the discharge and charge process, respectively. These values are larger than those for bare MnO (3.65×10^{-13} and $1.59 \times 10^{-14} \text{ cm}^2 \text{ s}^{-1}$, Fig. S9†).

The lithium ion diffusion coefficient can also be calculated from the EIS spectra. Fig. 4d shows the Nyquist plots of the bare MnO and 3DCG/MnO electrodes. The intercept of the high frequency semicircle on the Z' axis can be ascribed to the internal resistance, denoted as R_e in the equivalent circuit (Fig. 4e), which includes electrolyte resistance, particle–particle contact resistance, and resistance between the electrode and the current electrode. Moreover, each plot comprises a semicircle in the high frequency region related to the resistance of lithium ion migration through the SEI film (R_f), a medium frequency semicircle attributed to the charge transfer resistance (R_{ct}), and a slope line in low frequency region corresponding to the Warburg impedance (Z_w) of the lithium ion diffusion within the bulk electrode. The fitted R_f and R_{ct} values for the bare MnO electrode are 168.7 and 140.6 Ω , respectively, while for the 3DCG/MnO electrode they decrease to 4.8 and 34.5 Ω , implying much faster lithium ion adsorption, electron transfer, and lithium ion permeation at the electrode/electrolyte interface, resulting in better electrochemical kinetics. This result coincides with a smaller degree of polarization (Fig. S5 and S7†) and better electrochemical performance (Fig. 3c and d) of the 3DCG/MnO electrode. Moreover, the resistance at the

low frequency region shows a linear response to $\omega^{1/2}$, which can be described as follows:³⁶

$$Z' = K + \sigma\omega^{-1/2} \quad (3)$$

where K is a constant, ω is the frequency, and σ is the Warburg factor which corresponds to the slope of the curve shown in Fig. 4f. Hence, the lithium ion diffusion coefficient of the electrodes can be calculated according to the following equation:¹²

$$D = \frac{R^2 T^2}{2A^2 n^4 F^4 C^2 \sigma^2} \quad (4)$$

where D , R , T , A , and n correspond to the diffusion coefficient, gas constant, absolute temperature, total surface area of electrode, and charge transfer number, respectively. F is the Faraday constant and C is the molar concentration of lithium ions in MnO. Therefore, the estimated lithium ion diffusion coefficient for 3DCG/MnO ($2.76 \times 10^{-12} \text{ cm}^2 \text{ s}^{-1}$) is much higher than that for bare MnO ($3.78 \times 10^{-14} \text{ cm}^2 \text{ s}^{-1}$), suggesting that the electronic and ionic conductivity of the 3DCG/MnO electrode is enhanced through the construction of an interconnected 3D porous architecture.

To examine the structural stability of the 3D porous MnO-based anode material, SEM and TEM analyses were conducted on the 3DCG/MnO electrode after the cycling test (Fig. 5). As shown in Fig. 5a and b, the porous structure of the 3DCG/MnO composite can be maintained and the manganese oxide nanoparticles are still well-decorated on graphene, which is consistent to that of the pristine electrode (Fig. 2a). TEM observations further reveal that ultrafine manganese nanograins are homogeneously dispersed on the surface of graphene after cycling at a discharge state (Fig. 5c and d). The well-preserved morphology of the 3DCG/MnO electrode after cycling indicates that the conductive carbon networks could effectively accommodate the volume change in the active materials during the

repeated cycling and that the detachment of the active materials could be avoided. Moreover, the robust structure of the rationally designed 3DCG/MnO architecture is desirable for highly durable and cycle-stable LIBs, and can be attributed to the synergistic effect of the intrinsic porous structure and the MnO nanoparticles in the following ways. (1) The MnO nanoparticles are homogeneously embedded in the cross-linked CNT/graphene networks, forming a 3D porous interconnected architecture with a high specific surface area. The MnO nanoparticles in the 3D structure shorten the ion diffusion pathways, facilitating the conversion reaction kinetics. (2) The stable interpenetrated 3D porous architecture with abundant well-developed pores provides 3D pathways for lithium ion transfer and electrolyte storage, as well as ensuring full contact between the electrode and electrolyte. (3) The CNTs and graphene being combined builds a 3D conductive matrix which can effectively alleviate volume expansion and present the aggregation and pulverization of MnO nanoparticles during cycling, which is conducive to highly durable and cycle-stable lithium storage.

4 Conclusions

In summary, well-designed 3DCG/MnO architecture is rationally realized through a hydrothermal method and a subsequent solvothermal process, in which ultrafine MnO nanoparticles are homogeneously dispersed on a 3D cross-linked CNT/graphene matrix. Benefiting from unique structural characteristics and the synergistic effect between the MnO nanoparticles and the 3D porous conductive scaffold, the as-built 3DCG/MnO composite yields superior lithium storage performance, and in particular an outstanding cycling stability with a capacity retention of 98% after 1400 cycles at 2.0 A g^{-1} . It is believed that the remarkable cycling stability of 3DCG/MnO make it a promising anode material for electrochemical energy storage applications.

Conflicts of interest

There are no conflicts to declare.

Acknowledgements

This work was financially supported by the National Key Research and Development Program of China (Grant No. 2017YFA0303403), the Natural Science Foundation of China (Grant No. 61674057, 61504156, and 61227902), the Projects of Science and Technology Commission of Shanghai Municipality (Grant No. 18JC1412400 and 15JC1401600), and the Program for Professor of Special Appointment (Eastern Scholar) at the Shanghai Institutions of Higher Learning and the Fundamental Research Funds for the Central Universities.

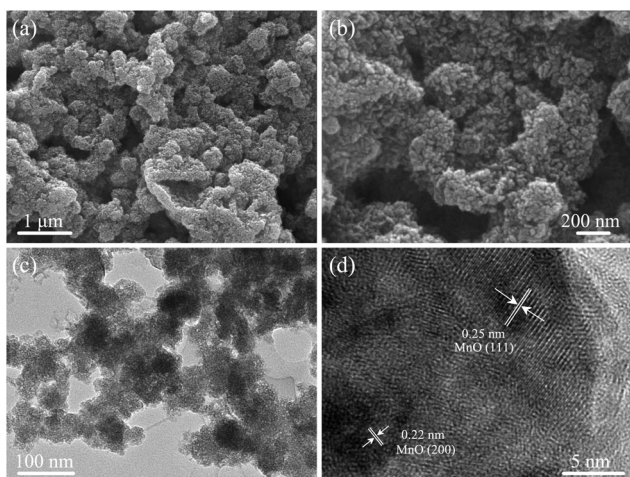


Fig. 5 Electrode morphology and structure after cycling: (a–b) SEM images of the 3DCG/MnO electrode after the cycling test; (c) TEM image of the 3DCG/MnO electrode after cycling; (d) HRTEM image of 3DCG/MnO after cycling.

References

- J. B. Goodenough, *Energy Environ. Sci.*, 2014, **7**, 14–19.
- P. Simon, Y. Gogotsi and B. Dunn, *Science*, 2014, **343**, 1210–1211.
- H. Wu, G. Yu, L. Pan, N. Liu, M. T. McDowell, Z. Bao and Y. Cui, *Nat. Commun.*, 2013, **4**, 1943–1948.
- Y. Idota, T. Kubota, A. Matsufuji, Y. Maekawa and T. Miyasaka, *Science*, 1997, **276**, 1395–1397.
- L. Zhang, H. B. Wu and X. W. Lou, *Adv. Energy Mater.*, 2014, **4**, 1300958.
- Y. Xia, Z. Xiao, X. Dou, H. Huang, X. H. Lu, R. J. Yan, Y. P. Gan, W. J. Zhu, J. P. Tu, W. K. Zhang and X. Y. Tao, *ACS Nano*, 2013, **7**, 7083–7092.
- W. Zhang, J. Z. Sheng, J. Zhang, T. He, L. Hu, R. Wang, L. Q. Mai and S. C. Mu, *J. Mater. Chem. A*, 2016, **4**, 16936–16945.
- L. L. Zhang, D. H. Ge, G. L. Qu, J. W. Zheng, X. Q. Cao and H. W. Gu, *Nanoscale*, 2017, **9**, 5451–5457.
- Y. M. Sun, X. L. Hu, W. Luo, F. F. Xia and Y. H. Huang, *Adv. Funct. Mater.*, 2013, **23**, 2436–2444.
- W. Zhang, J. Z. Sheng, J. Zhang, T. He, L. Hu, R. Wang, L. Q. Mai and S. C. Mu, *J. Mater. Chem. A*, 2016, **4**, 16936–16945.
- W. Zhang, J. N. Li, J. Zhang, J. Z. Sheng, T. He, M. Y. Tian, Y. F. Zhao, C. J. Xie, L. Q. Mai and S. C. Mu, *ACS Appl. Mater. Interfaces*, 2017, **9**, 12680–12686.
- J. Zhang, W. Zhang, T. He, I. S. Amiinu, Z. K. Kou, J. N. Li and S. C. Mu, *Carbon*, 2017, **115**, 95–104.
- H. Jiang, Y. J. Hu, S. J. Guo, C. Y. Yan, P. S. Lee and C. Z. Li, *ACS Nano*, 2014, **8**, 6038–6046.
- L. F. Chen, S. X. Ma, S. Lu, Y. Feng, J. Zhang, S. Xin and S. H. Yu, *Nano Res.*, 2017, **10**, 1–11.
- W. Wei, S. Yang, H. Zhou, I. Lieberwirth, X. Feng and K. Müllen, *Adv. Mater.*, 2013, **25**, 2909–2914.
- Q. Zhang, J. Wang, J. Dong, F. Ding, X. Li, B. Zhang, S. Yang and K. Zhang, *Nano Energy*, 2015, **13**, 77–91.
- Y. F. Dong, M. L. Yu, Z. Y. Wang, Y. Liu, X. Z. Wang, Z. B. Zhao and J. S. Qiu, *Adv. Funct. Mater.*, 2016, **26**, 7590–7598.
- T. Z. Yuan, Y. Z. Jiang, W. P. Sun, B. Xiang, Y. Li, M. Yan, B. Xu and S. X. Dou, *Adv. Funct. Mater.*, 2016, **26**, 2198–2206.
- Y. Zhang, P. H. Chen, X. Gao, B. Wang, H. Liu, H. Wu, H. K. Liu and S. X. Dou, *Adv. Funct. Mater.*, 2016, **26**, 7754–7765.
- J. R. He, Y. F. Chen, P. J. Li, F. Fu, Z. G. Wang and W. L. Zhang, *J. Mater. Chem. A*, 2015, **3**, 18605–18610.
- Y. Xiao and M. H. Cao, *ACS Appl. Mater. Interfaces*, 2015, **7**, 12840–12849.
- Q. Sun, Z. J. Wang, Z. J. Zhang, Q. Yu, Y. Qu, J. Y. Zhang, Y. Yu and B. Xiang, *ACS Appl. Mater. Interfaces*, 2016, **8**, 6303–6308.
- Z. Cui, Q. Liu, C. T. Xu, R. J. Zou, J. H. Zhang, W. L. Zhang, G. Q. Guan, J. Q. Hu and Y. G. Sun, *J. Mater. Chem. A*, 2017, **5**, 21699–21708.
- J. G. Wang, D. D. Jin, H. Y. Liu, C. B. Zhang, R. Zhou, C. Shen, K. Y. Xie and B. Q. Wei, *Nano Energy*, 2016, **22**, 524–532.
- D. H. Liu, H. Y. Lu, X. L. Wu, B. H. Hou, F. Wan, S. D. Bao, Q. Y. Yan, H. M. Xie and R. S. Wang, *J. Mater. Chem. A*, 2015, **3**, 19738–19746.
- J. G. Wang, C. B. Zhang, D. D. Jin, K. Y. Xie and B. Q. Wei, *J. Mater. Chem. A*, 2015, **3**, 13699–13705.
- J. Y. Wang, Q. L. Deng, M. J. Li, K. Jiang, Z. G. Hu and J. H. Chu, *Nanoscale*, 2018, **10**, 2944–2954.
- Q. T. Zhang, Q. Q. Dai, M. Li, X. M. Wang and A. Li, *J. Mater. Chem. A*, 2016, **4**, 19132–19139.
- L. Liu, X. F. Yang, C. X. Lv, A. M. Zhu, X. Y. Zhu, S. J. Guo, C. M. Chen and D. J. Yang, *ACS Appl. Mater. Interfaces*, 2016, **8**, 7047–7053.
- M. J. Li, Q. L. Deng, J. Y. Wang, K. Jiang, Z. G. Hu and J. H. Chu, *Nanoscale*, 2018, **10**, 741–751.
- J. Hassoun, K. S. Lee, Y. K. Sun and B. Scrosati, *J. Am. Chem. Soc.*, 2011, **133**, 3139–3143.
- Y. Sun, H. W. Lee, Z. W. Seh, N. Liu, J. Sun, Y. Li and Y. Cui, *Nat. Energy*, 2016, **1**, 15008.
- H. Lindström, S. Södergren, A. Solbrand, H. Rensmo, J. Hjelm, A. Hagfeldt and S. E. Lindquist, *J. Phys. Chem. B*, 1997, **101**, 7717–7722.
- V. Ramar and P. Balaya, *Phys. Chem. Chem. Phys.*, 2013, **15**, 17240–17249.
- L. L. Peng, X. Zhang, Z. W. Fang, Y. Zhu, Y. J. Xie, J. J. Cha and G. H. Yu, *Chem. Mater.*, 2017, **29**, 10526–10533.
- P. Yu, B. N. Popov, J. A. Ritter and R. E. White, *J. Electrochem. Soc.*, 1999, **146**, 8–14.